Hyun-Cheol Song, Deepam Maurya, Jinsung Chun, Yuan Zhou, Myung-Eun Song, David Gray, Nana Kwame Yamoah, Dhananjay Kumar, Austin McDannald, Menka Jain and Shashank Priya*

Modulated Magneto-Thermal Response of $La_{0.85}Sr_{0.15}MnO_3$ and $(Ni_{0.6}Cu_{0.2}Zn_{0.2})Fe_2O_4$ Composites for Thermal Energy Harvesters

DOI 10.1515/ehs-2016-0016

Abstract: The magneto-thermoelectric generator (MTG) converts wasted thermal energy into electrical energy in two steps. The first step involves thermal to mechanical energy conversion through balance of magnetic and elastic forces and the second step involves mechanical to electrical energy conversion through piezoelectric effect. The requirements for soft magnetic material in improving the efficiency of first step were identified and met through the design of a composite architecture. The Curie temperature of $La_{(1-x)}Sr_xMnO_3$ can be engineered to be near room temperature by modifying the Sr content. Composite of $La_{0.85}Sr_{0.15}MnO_3$ (LSMO) and $Ni_{0.6}Cu_{0.2}Zn_{0.2}Fe_2O_4$ (NCZF) was found to exhibit high saturation (M_s) and remnant (M_r) magnetization magnitude while maintaining the soft magnetic nature. Two-step sintering was found to prevent the inter-diffusion of LSMO and NCZF phases and provided high density without grain growth. The LSMO-NCZF (70:30 *wt*%) composite exhibited a large variation in M_s with respect to the change in temperature near Curie temperature which meets the requirements for efficient operation of MTG. The fabricated MTG using LSMO-NCZF (70:30 *wt*%) composite reached 0.2 Hz operational frequency and generated electrical output voltage of $2\,V_{p-p}$ and peak power of 17 μW under the thermal gradient of 80 °C (0 °C/80 °C).

Keywords: magneto-thermoelectric generator, two-step sintering, LSMO, NCZF, magnetic composite

***Corresponding author: Shashank Priya,** Center for Energy Harvesting Materials and System (CEHMS), Bio-Inspired Materials and Devices Laboratory (BMDL), Virginia Tech, VA 24061, USA, E-mail: spriya@vt.edu
Hyun-Cheol Song: E-mail: songhc@vt.du, **Deepam Maurya:** E-mail: mauryad@vt.edu, **Jinsung Chun:** E-mail: jinsc83@vt.edu, **Yuan Zhou:** E-mail: yzhou6@vt.edu, **Myung-Eun Song:** E-mail: songme@vt.edu, Center for Energy Harvesting Materials and System (CEHMS), Bio-Inspired Materials and Devices Laboratory (BMDL), Virginia Tech, VA 24061, USA
David Gray, Prime Photonics, 1116 S Main St, Blacksburg, VA 24060, USA, E-mail: david.gray@primephotonics.com
Nana Kwame Yamoah: E-mail: nanakay@vt.edu, **Dhananjay Kumar:** E-mail: dkumar@ncat.edu, Department of Mechanical Engineering, North Carolina A&T State University, Greensboro, NC 27411, USA
Austin McDannald, Materials Science and Engineering Department, University of Connecticut, Storrs, CT 06269, USA, E-mail: austin.mcdannald@uconn.edu
Menka Jain, Department of Physics and Institute of Material Science, University of Connecticut, Storrs, CT 06269, USA, E-mail: menka.jain@uconn.edu

Introduction

In last few decades, thermoelectric generators have been the focus for converting thermal energy into electrical energy (Priya and Inman 2009; Hicks and Dresselhaus 1993; Terasaki, Sasago, and Uchinokura 1997; Chen et al. 2003; Hsu et al. 2004; Hochbaum et al. 2008; Gaultois et al. 2010; Shakouri 2011). The performance of thermoelectric device depends upon the figure of merit of the material, *ZT*, where *Z* is a measure of a material's electrical and thermal properties and *T* is the absolute temperature. Most of bulk thermoelectric materials show *ZT* values lower than 1 at room temperature, although there has been report of ZT = ~ 2.4 at 300 K in thermoelectric thin film with superlattice structure (Li et al. 2010; Venkatasubramanian et al. 2001). However, thermoelectric devices even with these high *ZT* values require large temperature gradient (Carnot's efficiency is related to difference in hot and cold side temperature) in the material to achieve high output power. It is challenging to preserve the large temperature differential within thermoelectric devices because of the lack of thermal dissipation and radiative losses. It is even more challenging to find sustainable large temperature gradient in the surrounding environment conducive for energy harvesting for wireless sensors. Therefore, practical implementation of thermoelectric devices near room temperature has been limited.

To overcome these problems of thermoelectric devices, magneto-thermoelectric generator (MTG) concept has been proposed which exploits the thermally induced second order phase transition of soft magnetic material at

their Curie temperature (T_C) (Ujihara, Carman, and Lee 2007; McCarthy, Marinero, and Fisher 2012; Joshi and Priya 2013). The MTG is composed of two main parts; an actuating part and heat exchanger. The actuating part consists of a bimorph piezoelectric cantilever structure (piezoelectric layers applied on both side of metal shim) and a soft magnet which is placed at the end of the cantilever as shown in Figure 1. The actuating part is kept between the heat exchanger comprising of cold sink and hot source as described in Figure 1. The hard magnet is attached to the hot source and it attracts the soft magnet mounted on the cantilever. At the beginning of operation, soft magnet is attracted to the hard magnet attached to the hot source. When the soft magnet is heated above its T_C, it transitions into the paramagnetic state and loses the attraction force. At that instant, the elastic forces from the cantilever detaches it from the hard magnet surface and returns it back towards the cold sink. Upon contacting the cold surface, the soft magnet again cools below T_C and transforms into ferromagnetic state. Thus, it once again gets attracted towards the hard magnet surface due to magnetic force of attraction. This continuous heat exchanging cycle repeats until the hot source temperature is maintained above certain threshold with respect to T_C of the soft magnet. During this continuous cycle, the soft magnet periodically oscillates at a fixed frequency and the mechanical energy is converted into electric energy through piezoelectric elements attached/deposited on the cantilever.

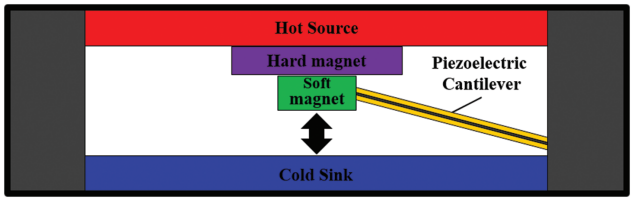

Figure 1: Schematic structure of MTG.

To efficiently operate the MTG, the fundamental challenge lies in synthesizing suitable soft magnetic materials that exhibit high magnetization change at T_C. Further, the soft magnetic material can be easily magnetized by the external magnetic field. To operate MTG near room temperature, the T_C of soft magnetic material should be close to the room temperature while maximizing the saturated (M_s) and remnant (M_r) magnetization with small coercive field (H_c). The magnetic force between the hard and soft magnet (Figure 1(d)) can be expressed as (Joshi and Priya 2013):

$$F_{mag} = \int_V M \nabla B_{mag} dV = -\int_V (\nabla \cdot \mathrm{M}) B_{mag} dV + \int_S \mathrm{M} B_{mag} dS = \int_V \rho_{mag} B_{mag} dV + \int_S \sigma_{mag} B_{mag} dS \quad [1]$$

Here, $\rho_{mag} = -\nabla \cdot M$ = volume (magnetic) charge density, $\sigma_{mag} = M$ = surface (magnetic) charge density. Thus, magnetic force is function of magnetization M and gradient of magnetization $\nabla \cdot M$ that in turn are function of temperature and temperature gradient respectively. The force in z-direction, assuming temperature is uniform throughout cross-section, can be determined as:

$$F_{mag}(z) = -A_{Gd} \int_{w_m}^{w_m + th} \frac{dM}{dz} B_{mag}(z) dz + A_{Gd}\big(M(w_m + th) B_{mag}(w_m + th) - M(w_m) B_{mag}(w_m)\big) \quad [2]$$

Equations [1] and [2] show that the gradient in magnetization of the soft magnet along with the B-magnetic field of hard magnet as function of distance z from the surface are critical parameters. In this study, we engineered the composite material architecture based upon $La_{0.85}Sr_{0.15}MnO_3$ (LSMO) and $Ni_{0.6}Cu_{0.2}Zn_{0.2}Fe_2O_4$ (NCZF) that is able to meet the above mentioned requirements for continuous operation of MTG near room temperature.

Experimental Details

$La_{(1-x)}Sr_xMnO_3$ ceramics with composition $0.15 \le x \le 0.30$ were prepared using high purity (>99 %) oxide precursors through conventional solid-state reaction. These oxide compounds La_2O_3, $SrCO_3$ and MnO_2 (Sigma-Aldrich, St. Louis, USA, >99 %) were ball milled under high purity ethanol for 24 h in a nylon jar with zirconia balls as milling media. After ball-milling, the slurry was dried and calcined at 850 °C for 3 h. After calcination, the resulting powders were further ball milled for 24 h followed by drying in an oven. The dried powders were sieved and pressed uniaxially into cylindrical pellets followed by sintering at 1,300 °C for 2 h. We synthesized Ni–Cu–Zn ferrite having composition of $Ni_{0.6}Cu_{0.2}Zn_{0.2}Fe_2O_4$ (NCZF) using conventional solid-state reaction with NiO, CuO, ZnO and Fe_2O_3 (Sigma-Aldrich, >99 %) as precursors. The calcination and sintering temperatures for NCZF were selected to be 750 °C (5 h) and 900 °C (2 h), respectively. The sintered NCZF powder was crushed and ball-milled for 48 h to achieve fine powder. In order to make LSMO-NCZF magnetic composite system, different amounts of NCZF

powder were mechanically mixed with the LSMO powder. These mixed powders were uniaxially pressed into cylindrical pellets followed by isostatic pressing under 200 MPa. The composite green pellets were sintered using two-step heating method in order to prevent the inter diffusion of LSMO and NCZF phases (Chen and Wang 2000; Wang et al. 2006a). The LSMO-NCZF composite samples were first heated at the rate of 10 °C/min up to 1,075 °C followed by rapid cooling to a lower temperature of 1,025 °C at the rate of 200 °C/min for isothermal sintering with a dwell time of 8 h. The phase formation and microstructure of specimens was examined by X-ray diffraction (XRD, Brucker, D8 Advance) and field-emission scanning electron microscopy (FESEM, LEO (Zeiss) 1550), respectively. The composition of various specimens was investigated through energy-dispersive spectroscopy (EDS). The magnetic domain configuration was observed using magnetic force microscopy (MFM, Brucker, Dimension FastScan). For quantifying magnetic properties, vibrating sample magnetometer (VSM) attached to the evercool physical property measurement system (PPMS, Quantum Design) was used.

The two-step sintered soft magnetic material was machined to rectangular shape of $8.7 \times 5.4 \times 0.4\,mm^3$ dimension. To reduce surface thermal contact resistance, a silver electrode was coated on both side of the soft magnetic material. The fabricated soft magnetic material was attached on a bimorph piezoelectric cantilever beam using super glue as shown in Figure 7(b). The bimorph piezoelectric cantilever consisted of 200 µm thickness platinized PVDF films (Kureha Inc.) assembled on 30 µm steel shim by double sided tape. In order to prevent voltage cancelation, poling direction of PVDF films were opposite to each other. The testing set up for the hot source and cold sink was designed using thermoelectric modules as heater and cooler. Cooling fan was added on cold-side to maintain the temperature steady. Neodymium (Nd) based permanent magnet was attached on the hot-side using conductive silver epoxy for efficient heat transfer. The moving part of the piezoelectric cantilever beam was fixed between thermoelectric heater and cooler. The gap distance between cold-side and the hard magnet was fixed at 6 mm. The operation test of MTG using the LSMO-NCZF composite was conducted using experimental set-up shown in Figure 7(a).

Results and Discussion

Figure 2(a) shows the temperature-dependent magnetization of $La_{(1-x)}Sr_xMnO_3$ ceramics in terms of strontium content (x) variation from 0.15 to 0.30. The magnetization curves were measured after field cooling at 100 Oe. The T_C was derived from the M–T curves by determining the intersection on the T-axis by the tangent at the inflexion point. The T_C of $La_{(1-x)}Sr_xMnO_3$ ceramics gradually increased from 310 K to 370 K with increase of strontium content (x). The variation of the T_C in perovskite lanthanum manganite is directly related to concentration of tetravalent manganese ion (Mn^{4+}) in the lattice (Jonker and Van Santen 1950). This can be attributed to the fact that Mn^{4+} ions can improve the double-exchange (DE) interaction (Zener 1951; Anderson and Hasegawa 1955; De Gennes 1960) between heterovalent ion (Mn^{3+}, Mn^{4+}) neighbors in the manganite lattice (Ramirez 1997). The

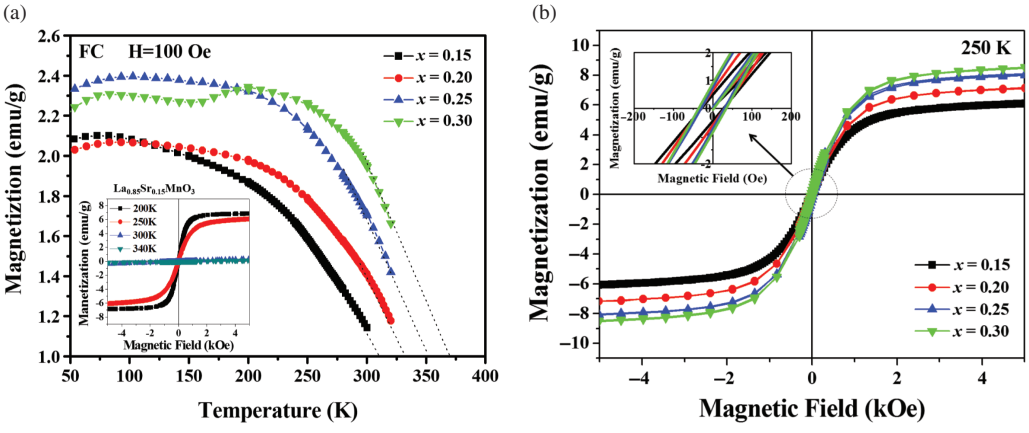

Figure 2: (a) Field-cooled (FC) temperature-dependent magnetization of $La_{(1-x)}Sr_xMnO_3$ in the $0.15 \le x \le 0.30$ strontium content range with applied field of 100 Oe. The inset shows magnetization vs. applied magnetic field (M-H hysteresis curves) data of $La_{0.85}Sr_{0.15}MnO_3$ at various temperatures. (b) M-H hysteresis curves of $La_{(1-x)}Sr_xMnO_3$ with variation of Sr content at 250 K. The inset shows zoomed view of hysteresis curves.

increased exchange interaction could elevate binding force between the magnetic ions and consequently the T_C. According to Jonker and Van Santen (1950), the amount of Mn^{4+} in $La_{(1-x)}Sr_xMnO_3$ ceramics can be increased by increasing the La^{3+} substitution on Sr^{2+} site up to about 35 % Sr when fired in air atmosphere (Jonker and Van Santen 1950). In case of more than 35 % Sr content, it is possible to obtain higher concentration of Mn^{4+} by firing in pure oxygen atmosphere. Thus, the T_C of $La_{(1-x)}Sr_xMnO_3$ system can be engineered through control of Sr content and sintering atmosphere as shown by our results which is consistent with the previous studies.

Figure 2(b) shows the isothermal magnetization hysteresis with variation of Sr content (x) in $La_{(1-x)}Sr_xMnO_3$ at 250 K. The value of saturation magnetization (M_s) was increased from 6 emu/g (for $x = 0.15$) to 8.4 emu/g (for $x = 0.30$) with increasing Sr ratio. The increased value of M_s can be attributed to the increased exchange interaction owing to the increased Mn^{4+} ion concentration (Jonker and Van Santen 1950). As shown in inset of Figure 2(b), all M-H curves exhibited clear hysteresis behavior at low applied magnetic fields with coercive fields (H_c) of 27.5, 29, 30 and 35 Oe and remnant magnetization (M_r) values of 0.49, 0.63, 0.75 and 0.90 emu/g for $La_{(1-x)}Sr_xMnO_3$ with $x = 0.15$, 0.20, 0.25 and 0.30, respectively. These moderately low values of H_c and M_r are typical characteristics of a soft magnetic material. However, the M_s and M_r values of $La_{(1-x)}Sr_xMnO_3$ system were low and needed new approach to achieve the desired range for their applications in MTG.

The relative materials performance index (PI) for MTG can be defined by following equation,

$$PI = \frac{(M_{s,\,Tc} - M_{s,\,T1})}{(T_C - T_1)} \qquad [3]$$

where T_C is Curie temperature, T_1 is applied temperature gradient for MTG, $M_{s,\,Tc}$ is saturated magnetization under constant magnetic field at T_C and $M_{s,\,T1}$ is saturated magnetization under constant magnetic field at T_1. The inset of Figure 2(a) shows the isothermal magnetization of $La_{0.85}Sr_{0.15}MnO_3$ composition at several temperatures. The PI of $La_{0.85}Sr_{0.15}MnO_3$ was found to be 0.116 emu/g·K under 5 kOe, calculated using the saturated magnetization value change from 250 K (ferromagnetic state) to 300 K (paramagnetic state). For successful operation of MTG, this value for the soft magnet should be improved significantly.

In order to achieve large M_s and M_r while maintaining soft magnetic nature, we engineered bulk composite of LSMO soft magnetic material with NCZF hard magnetic material. The LSMO composition has been chosen for the base matrix of magnetic composite due to its Tc close to room temperature. The NCZF powder was mechanically mixed with the LSMO powder in different weight ratios. It was found that if the compact of LSMO and NCZF mixture are sintered using normal heating schedule (1,200 °C for 2 h sintering, heating rate 5 °C/min) the manganese element in LSMO diffused into the NCZF phase as shown in EDS mapping images of Figure S1 (Supplementary Materials). As a result of this diffusion, the Tc was significantly decreased and magnetic properties also declined as shown in M-T curves of Figure S2 (Supplementary Materials). In order to maintain discrete phases of LSMO and NCZF in this composite system, we adopted two-step sintering approach (Chen and Wang 2000; Wang et al. 2006a). The two-step sintering suppresses the grain-boundary migration while keeping the grain boundary diffusion active. Therefore, through the two-step sintering, the inter-granular diffusion and grain growth can be suppressed while achieving higher packing density.

Figure 3(a) and (b) show the X-ray diffraction (XRD) patterns of pure LSMO and NCZF ceramics sintered at 1,300 °C and 950 °C for 2 h, respectively. The data shows that the homogeneous LSMO and NCZF phases were formed without any secondary phase. Figure 3(c)–(e) shows XRD patterns of LSMO-NCZF magnetic composites with different weight % of NCZF sintered using the two-step firing schedule, i. e., fired at 1,075 °C for short duration and then sintered at 1,025 °C for 8 h. The intensity of XRD peaks was found to increase gradually with the increase of NCZF content. The peaks for LSMO and

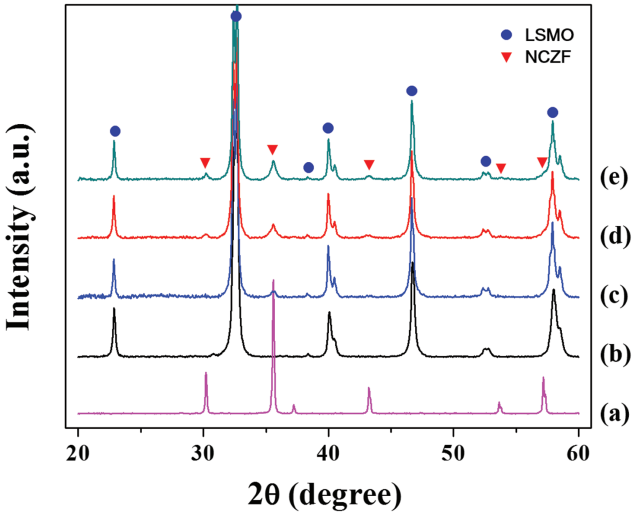

Figure 3: XRD patterns of (a) $Ni_{0.6}Cu_{0.2}Zn_{0.2}Fe_2O_4$, (b) $La_{0.85}Sr_{0.15}MnO_3$, (c) 90 *wt.* %LSMO-10 *wt.* %NCZF, (d) 80 *wt.* % LSMO-20 *wt.*NCZF, and (e) 70 *wt.* %LSMO-30 *wt.* %NCZF magnetic composites sintered by two-step schedule (1,075 °C = > 1,025 °C for 8 h).

NCZF phases in composites were distinct and no impurity phases were detected, which is clear evidence that inter-diffusion of LSMO and NCZF phases did not occur and high quality two phase ceramic composites were realized.

The SEM image of the surfaces of composite with 30 *wt.*% NCZF composition sintered by two-step schedule (1,075 °C, 1,025 °C for 8 h) is shown in Figure 4(a). Figure 4(b) shows an electron backscatter diffraction (EBSD) image of the morphology. A highly dense microstructure was formed and 96.7 % relative density was achieved by two-step sintering. The grain growth was suppressed by avoiding the grain boundary migration in the two-step sintering process. The relatively inhomogeneous size of grains might be attributed to the different size of initial powders of LSMO and NCZF. NCZF phase possessed larger grains than the LSMO as illustrated in Figure 4(a) and (b). In the second step of sintering process, there is not much change in the microstructure except for the reduction of porosity, because the grain boundary network is frozen. Therefore, the second step is important to achieve densification of the frozen microstructure. The normalized densification rate can be expressed as (Wang, Chen, and Chen 2006b):

$$\frac{d\rho}{\rho dt} = M(\rho)\frac{3sV}{k_B T}\frac{\delta D}{L^4} \quad [4]$$

where, s *is* surface energy, t is the time, k_B is the Boltzmann constant, T is the absolute temperature, V is the atomic volume, L is the mean grain size, δ is the grain boundary width, D is the grain boundary diffusivity, $M(\rho)$ is unspecified function of density (Wang, Chen, and Chen 2006b). To confirm the absence of the Mn diffusion from LSMO to NCZF phase, energy-dispersive spectroscopy (EDS) mapping was conducted on the two-step sintered LSMO-NCZF (70:30 *wt.*%) composite. Figure 4(c)–(e) show EDS mapping images for representative elements, Mn and Fe, in each phase. Both elements were homogeneously distributed over the entire surface of the specimen, as shown in Figure 4(d) and (e). However, the spatial arrangement of Mn and Fe elements was almost separated from each other as can be seen in Figure 4(c). The relatively ambiguous boundary of Mn and Fe elements in EDS mapping image could be attributed to the fact that the size of most grains (~ 200 nm) are smaller than the minimum useful detection spot size (~ 2 µm) of EDS as shown in the electron backscatter diffraction (EBSD) image of Figure 4(b). The separate distribution of Mn and Fe elements confirms that LSMO and NCZF phases were preserved during the sintering process. By employing a two-step sintering process, we achieved a dense microstructure and fine grains without inter diffusion in two phase ceramic composite system.

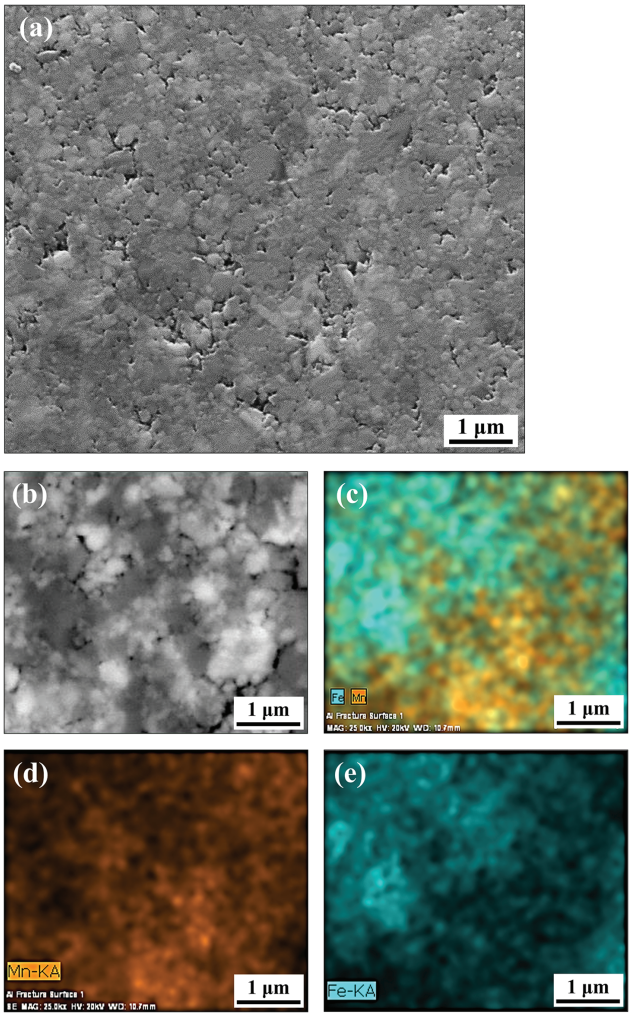

Figure 4: Two-step sintered LSMO-NCZF (70:30 *wt.*%) magnetic composite (a) SEM image, (b) EBSD image, (c) EDS mapping image for Fe and Mn elements, (d) EDS mapping image for Mn element and (e) EDS mapping image for Fe element.

In order to understand the magnetic domain and phase configuration of LSMO-NCZF composite, magnetic force microscopy (MFM) was conducted. MFM was performed below Curie temperature (at 290 K) of specimens to check the magnetic properties in ferromagnetic state. Figure 5(a) and (b) shows the topographic and magnetic phase images of two-step sintered 30 *wt*% NCZF magnetic composite, respectively. As shown in Figure 5(a) and (b), clear grain boundaries were observed and each phase had discrete and separated grains. As can be seen in Figure 5(b), the magnetic grains and clusters were clearly visible, however, the magnetic domains were not resolved owing to the discontinuous magnetic grain ordering in the lattice. The NCZF grains showed quite different contrast compared with LSMO grains because the NCZF grains with hard magnetic nature have

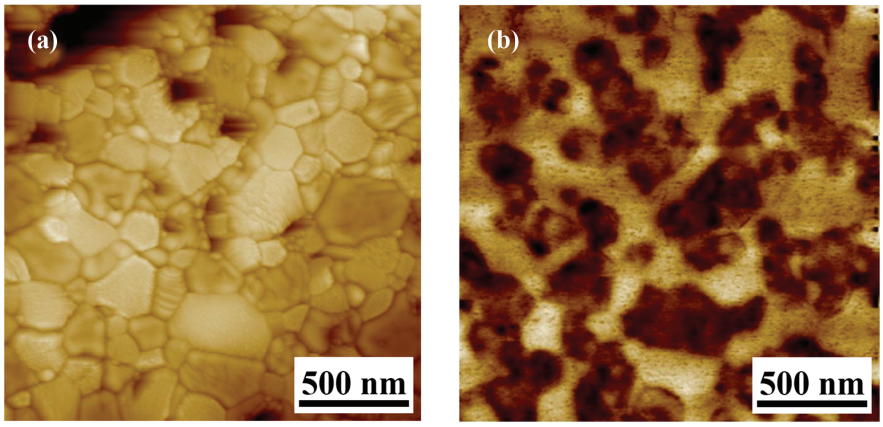

Figure 5: (a) Topographic and (b) MFM magnetic phase images of two-step sintered LSMO-NCZF (70:30 *wt.* %) magnetic composite.

higher magnetization. It can be assumed that the NCZF grains influence the LSMO matrix with soft magnetic properties by modulating the domain structure and magnetic response of the overall composite.

Figure 6(a) shows the temperature dependence of the magnetization (M–T) curves for the mixed powder and two-step sintered magnetic composite with 30 *wt.* % NCZF composition. The zero field-cooled (ZFC) curve was measured after cooling the specimen from 350 K down to 5 K without applying magnetic field. The field-cooled (FC) curve was obtained after initially cooling the specimen with an applied field of $H = 500$ Oe and then

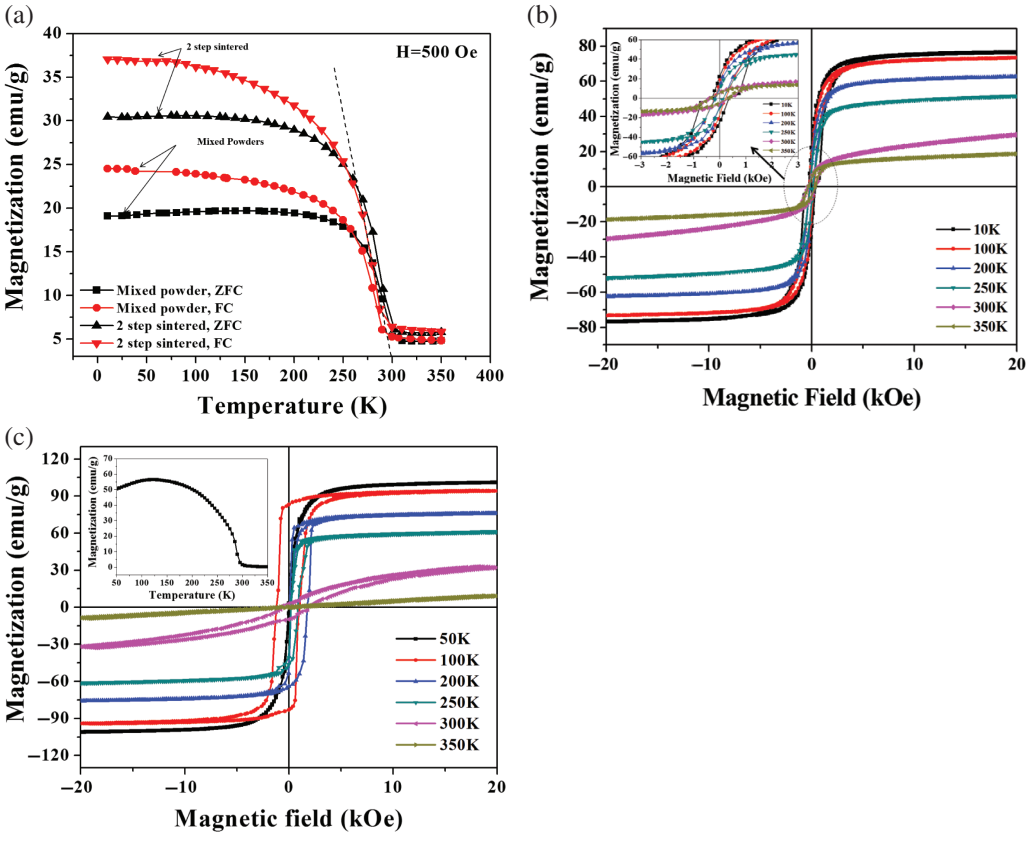

Figure 6: (a) The M-T curves of mixed powder and two-step sintered magnetic composite with LSMO-NCZF (70:30 *wt.* %) composition. (b) The M-H hysteresis curves of two-step sintered LSMO-NCZF (70:30 *wt.* %) magnetic composites with variation of temperature. Inset is zoomed view of hysteresis curves. (c) The M-H hysteresis curve of gadolinium (Gd) foil. Inset is the M-T curves of Gd foil with variation of temperature.

measured on heating. The ZFC and FC curves of the mixed powder and two-step sintered composite started to separate below 260 K, which indicates an irreversibility associated with the presence of magnetically disordered clusters in the lattice (Dörr 2006). The phase transition from paramagnetic to ferromagnetic phase was observed at *Tc* of 300 K in both cases. The *Tc* was reduced by 10 K compared to the pure LSMO which might be attributed to the presence of NCZF causing changes in the defect chemistry. The similarity of the temperature dependence of magnetic response in the composite and the mixture in Figure 6(a), indicates that the enhancement of magnetization comes from densification of the mixture. It is important to note that the magnetic nature of the mixture did not change after sintering and mainly densification was involved in the improvement of magnetization.

Figure 6(b) shows the M-H hysteresis curves for the two-step sintered 30 *wt.*% NCZF composite (with LSMO) at different temperatures. As shown in the inset of Figure 6(b), all isothermal magnetization loops showed clear hysteretic characteristics with soft magnetic nature at various temperatures. In particular, it is interesting to note that the curves above the *Tc* (300 K~) had a weak hysteretic characteristic, which may be attributed to the hard magnetic nature of NCZF phase existing in the matrix even though the LSMO lattice is in the paramagnetic state. Because of this reason, we could not increase NCZF content more than 30 %. The increasing hard magnetic nature above *Tc* will be problematic in operation of MTG as net gradient in magnetization is small resulting in incomplete detachment of the soft magnet from the hot-side magnet. It can be seen from the M-H curve at 250 K that the M_r and M_s values of the composite significantly improved to 9.6 emu/g

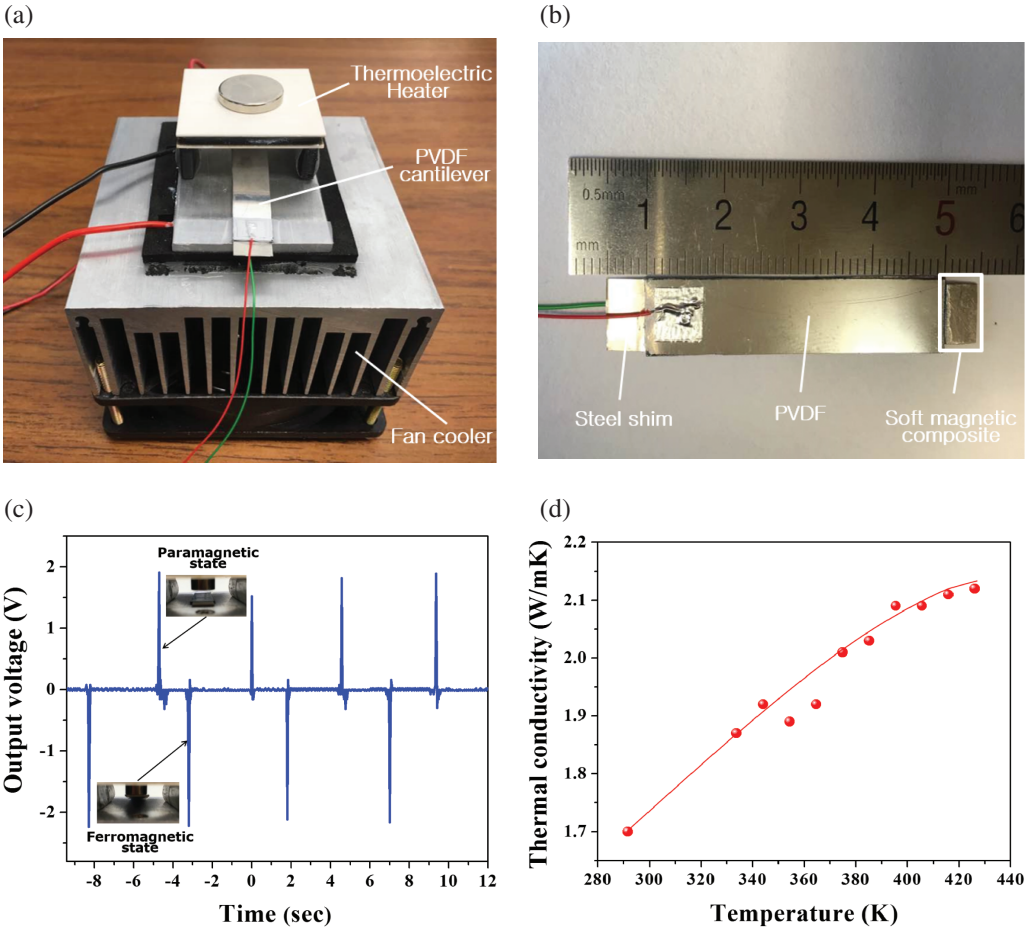

Figure 7: (a) MTG operation test set-up for the soft magnetic material. (b) Bimorph piezoelectric cantilever beam with LSMO–NCZF (70:30 *wt.*%) soft magnetic material developed in this study. (c) Generated output voltage by MTG using the LSMO–NCZF (70:30 *wt.*%) magnetic composite under 80 °C temperature gradient (0 °C/80 °C) (d) Thermal conductivity of two-step sintered LSMO-NCZF (70:30 *wt.*%) magnetic composites as function of temperature.

and 47 emu/g in comparison to that of 0.49 emu/g and 6 emu/g for pure-LSMO, respectively. On the other hand, the H_c value was only moderately increased from 27.5 Oe (for LSMO) to 178 Oe (for LSMO-30 wt% NCZF composite) owing to the hard magnetic nature of the NCZF. This can be explained by noticing that the overall magnetic response is average of the individual contributions from LSMO and NCZF phase proportional to their volume fraction (Kneller and Hawig 1991). The PI value estimated for the composite having 30 *wt.* % NCZF, considering M_s change in the range of 250 K–300 K (Figure 6(b)), was increased to 0.552 emu/g·K (at 5 kOe) in comparison with that of pure LSMO (0.116 emu/g·K). This value is still lower than 0.786 emu/g·K (at 5 kOe) of P.I. obtained for gadolinium (Gd) foil from M-H hysteresis curves in Figure 6(c). However, the LSMO-NCZF composites have advantage of tunable Curie temperature depending on the operation temperature with relative large P.I. value. This tunability is desired and makes LSMO-NCZF composite a potential candidate for soft magnetic materials in MTG.

Figure 7(a) shows the operation test set-up for MTG with a cantilever beam structure. The hot source and heat sink were created by using thermoelectric module. A cooling fan was attached under thermoelectric module to maintain continuous cooling condition. The soft magnet was attached at the end of bimorph PVDF cantilever beam as shown in Figure 7(b) and placed between hot and cold side. After applying electric field to thermoelectric module, the temperature gradient (ΔT) was induced and maintained at 80 °C (0 °C/80 °C). The gap distance between cold-side and hot-side hard magnet was maintained at 6 mm. In Figure 7(c), lower inset image, shows the ferromagnetic state of the soft magnetic material below its Curie temperature when it is attracted to the hot-side of the permanent magnet. Figure 7(c) upper inset image shows the paramagnetic state of soft magnet when it was detached from the permanent magnet and pulled towards the heat sink after losing magnetic force of attraction. This cycle of attraction and detachment was repeated by continuous ferromagnetic and paramagnetic phase change of the soft magnet at its Curie temperature. Figure 7(c) shows the generated output voltage at ΔT = 80 °C in MTG. The generated output voltage was approximately 2 V_{P-P} and the attraction to the magnet showed a larger output voltage than detachment. This is due to the higher attraction force by the magnet as compared to the releasing force by the cantilever. The generated maximum peak power was 17 μW at 1 MΩ. The operational frequency of the soft magnetic material was around 0.2 Hz. Thermal conductivity of soft magnetic composite as a function of temperature is shown in Figure 7 (d). From this data, it can be seen that thermal conductivity at Curie temperature (300 K) was low, on the order of 1.75 W/(*m*·K). The measured thermal conductivity increased with increasing temperature but was still lower than 8.0 W/(*m*·K) achieved for Gd metal at 300 K. In our future studies, higher thermal conducting material such as carbon nanotube or graphene will be incorporated inside the matrix of the magnetic material to enhance the overall thermal conductivity.

Conclusion

In summary, we have developed a soft magnetic composite that meets the requirement of magneto-thermal generator. The $La_{(1-x)}Sr_xMnO_3$ system where *Tc* can be modulated through varying Sr content (*x*) was modified with NCZF hard magnetic material for improving the M_s and M_r values while retaining its soft magnetic nature. The LSMO-NCZF ceramic composite was fabricated by two-step sintering in order to obtain full density without inter-phase diffusion. The structural, morphological, and compositional analysis indicated that the completely separated LSMO and NCZF grains with grain size below 200 nm were well developed. The LSMO-NCZF composite with 70:30 wt% ratio, exhibited significantly large variation in the saturated magnetization as a function of temperature change near its *Tc*. The fabricated MTG using this LSMO-NCZF composite showed 0.2 Hz operation frequency and generated maximum outputs of 2 V_{P-P} of output voltage and 17 μW of peak power under the thermal gradient of 80 °C.

Funding: The authors acknowledge the financial support through ARFL STTR Contract FA9550-13-C-0001 under management by Dr. Byung-Lip Lee. Author MJ is grateful for National Science Foundation grant (DMR # 1310149) for magnetic measurements. D.M. would like to acknowledge the support from Office of Basic Energy Sciences, Department of Energy (DE-FG02-06ER46290). J.S. was supported by AFOSR through grant FA9550-14-1-0376. S.P. acknowledges the financial support from Norfolk State University through NSF CREST program.

References

Anderson, P. W., and H. Hasegawa. 1955. "Considerations on Double Exchange." *Physical Review* 100:675.

Chen, G., M. S. Dresselhaus, G. Dresselhaus, J. -P. Fleurial, and T. Caillat. 2003. "Recent Developments in Thermoelectricmaterials." *International Materials Reviews* 48:45.

Chen, I. -W., and X. -H. Wang. 2000. "Sintering Dense Nanocrystalline Ceramics Without Final-Stage of Grain Growth." *Nature* 404:168.

De Gennes, P. -G. 1960. "Effects of Double Exchange in Magnetic Crystals." *Phys. Rev* 118:141.

Dörr, K. 2006. "Ferromagnetic Manganites-Spin Polarized Conduction vs Competing Interations." *Journal of Physics D: Applied Physics* 39:R125.

Gaultois, M. W., T. D. Sparks, C. K. H. Borg, R. Seshadri, W. D. Bonificio, and D. Clarke. 2010. "Data-Driven Review of Thermoelectric Materials: Performance and Resource Consideration." *Chemistry of Materials* 25:2911.

Hicks, L. D., and M. S. Dresselhaus. 1993. "Effect of Quantum-Well Structures on the Thermoelectric Figure of Merit." *Physical Review B* 47:12727.

Hochbaum, A. I., R. Chen, R. D. Delgado, W. Liang, E. C. Garnett, M. Najarian, A. Majumdar, and P. Yang. 2008. "Enhanced Thermoelectric Performance of Rough Silicon Nanowires." *Nature* 451:163.

Hsu, K. F., S. Loo, F. Guo, W. Chen, J. S. Dyck, C. Uher, T. Hogan, E. K. Polychroniadis, and M. G. Kanatzidis. 2004. "Cubic $AgPbmSbTe_2$ Bulk Thermoelectric Materials with High Figure of Merit." *Science* 303:818.

Jonker, G. H., and J. H. Van Santen. 1950. "Ferromagnetic Compounds of Manganese with Perovskite Structure." *Physica* 16:337.

Joshi, K. B., and S. Priya. 2013. "Multi-Physics Model of a Thermo-Magnetic Energy Harvester." *Smart Materials and Structures* 22:055005.

Kneller, E. F., and R. Hawig. 1991. "The Exchange-Spring Magnet: A New Material Principle for Permanent Magnets." *IEEE Transactions on Magnetics* 27:3588.

Li, J. -F., W. -S. Liu, L. -D. Zhao, and M. Zhou. 2010. "High-Performance Nanostructured Thermoelectric Materials." *NPG Asia Materials* 2:152.

McCarthy, P. T., E. E. Marinero, and T. S. Fisher. 2012. "Carbon Nanotube Thermal Interfaces on Gadolinium Foil." *International Journal of Heat and Mass Transfer* 55:6716.

Priya, S., and D. J. Inman. 2009. In *Energy Harvesting Technologies*, 1st ed, edited by S. Priya and D. J. Inman. NY: Springer.

Ramirez, A. P.. 1997. "Colossal Magnetoresistance." *Journal of Physics: Condensed Matter* 9:8171.

Shakouri, A. 2011. "Recent Developments in Semiconductor Thermoelectric Physics and Materials." *Annual Review of Materials Research* 41:399.

Terasaki, I., Y. Sasago, and K. Uchinokura. 1997. "Large Thermoelectric Power in $NaCo_2O_4$ Single Crystals." *Physical Review B* 56:R12 685.

Ujihara, M., G. P. Carman, and D. G. Lee. 2007. "Thermal Energy Harvesting Device Using Ferromagnetic Materials." *Applied Physics Letters* 91:093508.

Venkatasubramanian, R., E. Siivola, T. Colpitts, and B. O'Quinn. 2001. "Thin-Film Thermoelectric Devices with High Room-Temperature Figures of Merit." *Nature* 413:597.

Wang, X. -H., P. -L. Chen, and I. -W. Chen. 2006b. "Two-Step Sintering of Ceramics with Constant Grain-Size, I. Y_2O_3." *Journal of the American Ceramic Society* 89:431.

Wang, H., X. -Y. Deng, H. -L. Bai, H. Zhou, W. -G. Qu, L. -T. Li, and I. -W. Chen. 2006a. "Two-Step Sintering of Ceramics with Constant Grain-Size, II: $BaTiO_3$ and Ni–Cu–Zn Ferrite." *Journal of the American Ceramic Society* 89:438.

Zener, C. 1951. "Interaction Between the D Shells in the Transition Metals." *Physics Review* 81:440.